Turkish Journal of Science & Technology
Volume 12(2), 43-52, 2017

Effect of Heat Input on Microstructure, Friction and Wear Properties of Fe-Cr-B-C Coating on AISI 1020 Surface Coated by PTA Method

Turan GÜRGENÇ[1], Cihan ÖZEL[2]
[1]Firat University Technology Faculty Automotive Engineering Department, 23119 ELAZIĞ
[2]Firat University Engineering Faculty Mechanical Engineering Department, 23119 ELAZIĞ
tgurgenc@firat.edu.tr

(Geliş/Received:23.06.2017; Kabul/Accepted:06.09.2017)

Abstract

In this study, low carbon steel AISI 1020 surface was coated in different heat inputs with (%-wt.) 70FeCrC-30Fe B ferro alloy powder mixture by using plasma transferred arc (PTA) welding method. The microstructure of the coating layers were investigated by using optical microscope (OM), scanning electron microscope (SEM), X-ray diffraction (XRD) and energy dispersive X-ray (EDS). The dry sliding wear and friction properties were determined using a block-on-disc type wear test device. Wear tests were performed at 19.62 N, 39.24 N, 58.86 N load and the sliding distance of 900 m. The results were show that coated samples were consisted of mostly M_7C_3 (M=Cr, Fe) carbide, (Cr, Fe)B, FeB and Fe_2B boride. It was seen that the dendrites were growth with increasing heat input. The highest average microhardness value was measured 1096 HV on sample coated with low heat input. It was determined that the sample with the highest wear resistance was the sample coated by the low heat input.

Keywords: PTA welding, AISI1020, Fe-Cr-B-C coating, Wear, Friction.

PTA Yöntemiyle Kaplanan AISI 1020 Yüzeyine Fe-Cr-B-C Kaplamanın Mikroyapı, Sürtünme ve Aşınma Özelliklerine Isı Girdisinin Etkisi

Özet

Bu çalışmada, düşük karbonlu AISI 1020 çeliğinin yüzeyi farklı ısı girdilerinde (% ağ.) 70FeCr-C-30FeB ferro alaşım tozu karışımıyla plazma transfer ark (PTA) kaynak yöntemi kullanılarak kaplandı. Kaplama tabakalarının mikro yapıları optik mikroskop (OM), taramalı elektron mikroskobu (SEM), X ışını kırınımı (XRD) ve enerji dağılımlı X-ray (EDS) kullanılarak incelendi. Kuru kaymalı aşınma ve sürtünme özellikleri blok-on-disk tip aşınma test cihazı kullanılarak belirlendi. Aşınma testleri 19.62 N, 39.24 N, 58.86 N yükte ve 900 m kayma mesafesinde gerçekleştirildi. Sonuçlar, kaplanmış numunelerin genelde M_7C_3 (M=Cr, Fe) karbürü, (Cr, Fe)B, FeB ve Fe_2B borüründen oluştuğunu gösterdi. Dendritlerin artan ısı girdisiyle büyüdüğü görüldü. En yüksek ortalama mikro sertlik değeri düşük ısı girdisiyle kaplanan numunede 1096 HV olarak ölçüldü. En yüksek aşınma direncine sahip numunenin düşük ısı girdisi ile kaplanan numune olduğu tespit edildi.

Anahtar Kelimeler: PTA kaynak, AISI 1020, Fe-Cr-B-C kaplama, Aşınma, Sürtünme.

1. Introduction

Metallic machine parts expose to wear under working conditions, this causes significant loss of material per year [1]. Surface coating is the one of the most frequently used method for improving the wear of metal surfaces [2]. Welding is a method that use for depositing wear resistance materials on surface of metallic parts [3, 4]. The deposition of wear resistance materials on the surface with different welding methods such as plasma transferred arc (PTA) welding, gas tungsten arc welding (GTA) welding, oxyacetylene welding and laser welding have been widely used in industry to protect the metallic parts surfaces from wear [5-8]. High carbon and chromium content alloys are widely used in wear resistance required applications, such as mining, minerals, cement and paper industries [9]. Fe-Cr-C alloys are generally used as coating material, because of low price and high mechanical properties [10]. Fe-Cr-C alloys coating have excellent wear and corrosion resistance, because of comprising high hardness

carbides in the microstructure, such as M_3C, M_7C_3 and $M_{23}C_6$ [11]. Also Fe-Cr-B and Fe-Cr-B-C alloys coatings are known as high wear and corrosion resistance coatings [12-14].

In this study, 70FeCrC-30FeB ferro alloy powder mixture was coated on AISI 1020 steel in different heat inputs by using PTA welding method. The microstructure of the coating layers were analyzed with using OM, SEM, EDS and XRD. The microhardness, wear and friction coefficient properties of the coatings were determined. Finally worn surfaces were examined by using SEM microscope.

2. Material and Method

In this study, commercially provided AISI 1020 low carbon steel was used as substrate material. The substrate was prepared in dimensions as shown in Figure 1. High carbon content FeCrC and FeB ferro alloy powders were used as coating materials. The powders sizes are approximately 38 μm. In Table 1, the chemical composition of AISI 1020 steel and ferro alloy powders are given.

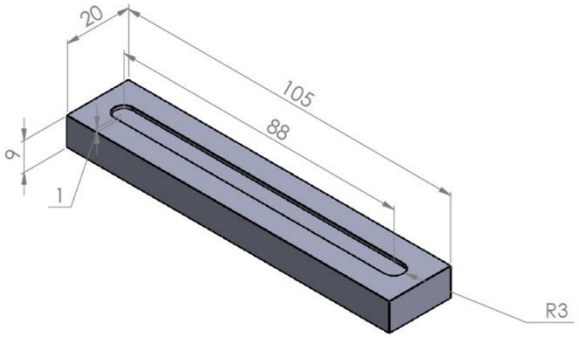

Figure 1. The dimensions of AISI 1020 (mm).

Table 1. Chemical compositions of AISI 1020 and ferroalloys (wt.-%).

Material	Cr	B	C	Mn	Fe	Other
AISI1020	-	-	0.2	0.356	Bal.	0.306
FeCrC	66.77	-	7.95	-	Bal.	0.557
FeB	-	18.22	0.3	-	Bal.	0.55

The surface of the substrate material was cleaned before coating with acetone after spraying the compressed air to clean the surface from oil and dirt. After that substrate was dried in the furnace at 60°C for 30 minutes in order to remove the moisture. The powders were dried in the furnace at 110 °C for 1 hour to remove the moisture of the coating powders. These powders, containing (%-wt.) 70FeCrC-30FeB, were weighed with a precision scale and a total of 30 g powder mixture was obtained for surface coating. This mixture was stirred for 1 hour at 150 rpm/min in a mechanical stirrer and it was placed in the opened channel on the substrate material. It was stuck to the surface with alcohol to prevent alloy powders from flying during welding. After this process, experimental samples were placed in the furnace to remove moisture and kept there at 100 °C for 1 hour for drying. After the samples had been removed from the furnace, they were kept until the room temperature was reached and the surface coating processes were carried out at different coating speeds and heat inputs using the Thermal Dynamics WC100B PTA welding device with the parameters given in Table 2. Argon was used as the plasma gas and shielding gas. After the coating process, the samples were put on to cool at room temperature.

Table 2. PTA coating parameters

Sample	S1	S2	S3	S4	S5	S6
Current (A)	120	140	160	120	140	160
Coating speed (m/min)	0.15	0.15	0.15	0.1	0.1	0.1
Voltage (V)	18-20					
Plasma gas flow rate (l/min)	0.5					
Shielding gas flow rate (l/min)	8					
Coating length (mm)	2					
Heat input (kj/mm)	0.475	0.585	0.704	0.713	0.878	1.056

Then, these samples were sanded with 60, 120, 180, 240, 400, 600, 800, 1000 and 1200 mesh SiC sandpaper, respectively, and then polished with using 3µm size of diamond paste. The polished samples were washed with alcohol and dried. After this process, the samples were etched for 2 minutes with a mixture of 15 g of $FeCl_3$, 15 ml of HCl and 100 ml of distilled water. The etched samples were cleaned with alcohol and dried with hot air after being washed with soap.

The etched coating surfaces were examined using an optical microscope (OM) and scanning electron microscope (SEM). The chemical composition of the compounds comprising the coating was determined by the energy-dispersive X-ray analysis (EDS) and the type of the compounds was determined by the X-ray diffraction (XRD) analysis. The hardness of the coating was measured by applying a force of 200 gf from the midpoint of the top surface of the coating to the main material at 0.25 mm intervals with a microhardness test device.

The samples required for the adhesive wear test were cut at 6x9x6 mm^3 from near the midpoint of the coated samples. Before the wear test, the coated surfaces of the samples were sanded with 400 mesh sandpaper and then cleaned with alcohol. Wear tests were carried out in a "block-on-disc" adhesive wear tester at a normal load of 19.62 N, 39.24 N and 58.86 N. AISI 52100 bearing steel 15 mm in diameter was used as the abrasive and the samples were worn at a total of 900 m sliding distance at each load. Weight losses were measured with a precision scale of 10-5 g precision at every 300 m. During the wear test, the change in friction force dependent on the sliding distance was recorded and transferred to the computer via a data logger. Finally, the worn coating surfaces were analyzed using a SEM microscope.

3. Results and Discussion

3.1. Microstructure

In Figure 2 and Figure 3 the macro photographs and interface images of the Fe-Cr-B-C coated samples were shown respectively. As seen from the test specimens there is no crack or porosity on the coated surfaces, interfaces and coating layers.

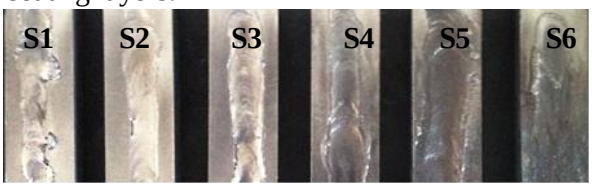

Figure 2. Macro photographs of the coated surfaces.

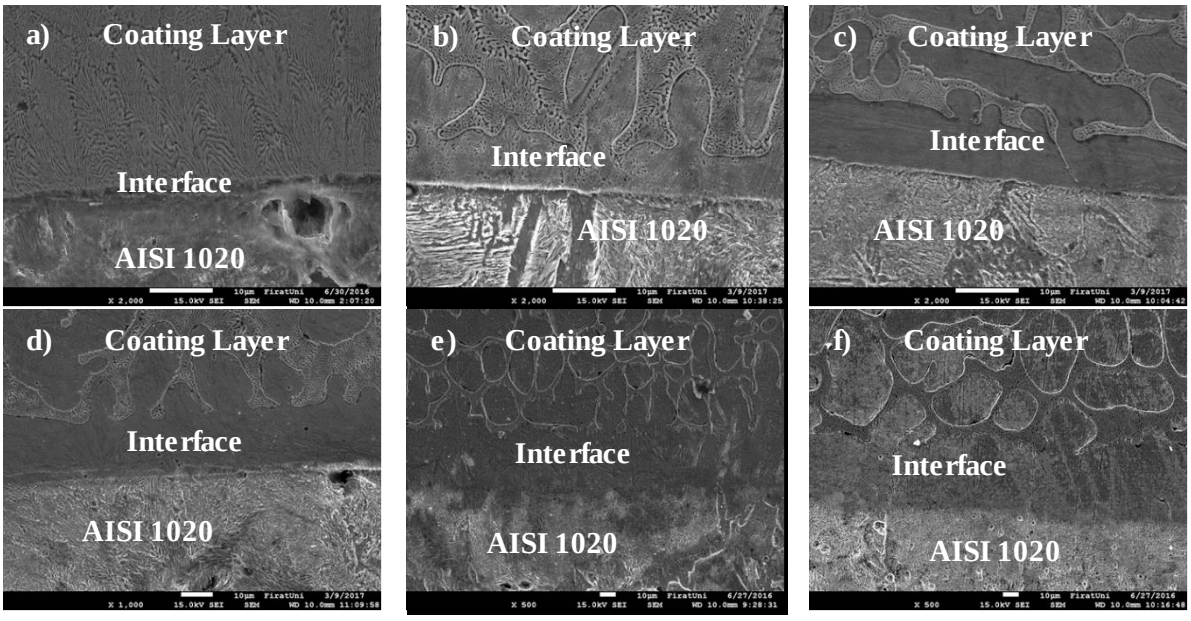

Figure 3. SEM images of coating interfaces **a)** S1 (x2000), **b)** S2 (x2000), **c)** S3 (x2000), **d)** S4 (x1000), **e)** S5 (x500) and **f)** S6 (x500).

The coating layers some properties were given in Table 3. As seen from the Table 3 coating layers depths and interface regions heights were increase with increasing heat input. The percentages of dendrites increased with increasing heat input because of intensive melting. Also with increasing heat input dendrites were growth.

Table 3. General properties of coating layers.

Sample	H	H_1	Dendrite	%P	Aav.	Wav.
S1	1410 µm	1.875 µm	-	-	-	-
S2	1470 µm	7.295 µm	Dendrite	31.5	75.2 µm2	6.2 µm
S3	1560 µm	9.975 µm	Dendrite	42	364.2 µm2	9 µm
S4	2170 µm	17.8 µm	Dendrite	45.6	486.6 µm2	16.8 µm
S5	3490 µm	38.31 µm	Dendrite	54.5	2561.7 µm2	31.1 µm
S6	4610 µm	42.33 µm	Dendrite	70.2	2621 µm2	34.2 µm

H: Coating maximum depth; **H_1**: Average interface height taken from five different points; **%P:** Percante of the dendrites; **Aav.:** Average area of the phases; **Wav.:** Average width of the phases

The boron and carbon ratios in the coating areas could not be determined by EDS analysis because of the atomic numbers were low. The boron containing compounds in the coatings were determined by the XRD analysis given in Figure 4. According to the XRD analysis results, all of the coating layers were generally composed of M_7C_3 (M=Cr, Fe) carbide, (Cr, Fe)B, FeB and Fe_2B borides. In addition to these phases a little amount of α-Fe and FeCr were detected. These structures were also observed in similar studies [15, 16].

The OM photographs of the coating layers are shown in Figures 5-10. As seen from the Figures, different microstructures appeared in the coating layers with the change of heat input. This can be explained by the change of the melting amount of the substrate material with the change of heat input and therefore the change of the chemical composition of the coating. As it seen from Figure 5a, borides and carbides in the coating layer are solidified as a colony because of the solidification time is short due to low heat input. The other samples (S2-S6) microstructures were consists of dendrites and interdendritic eutectic structures (Figure 6-10).

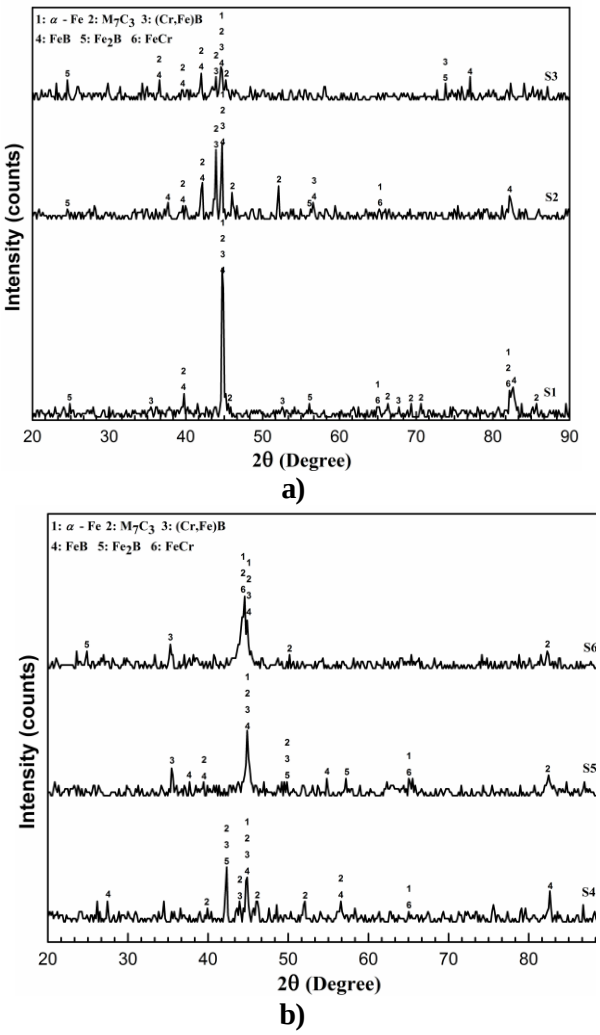

Figure 4. XRD results **a)** S1-S3 and **b)** S4-S6.

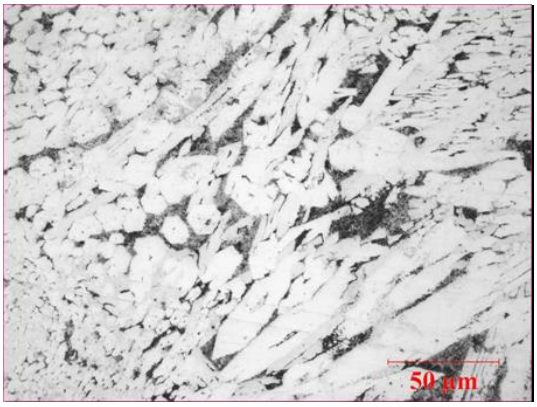

Figure 5. OM photograph of S1 x500.

The dendrite arms expand and stretch as the heat input increases. In addition, parallel to the increase of the heat input the dendrites occupy a

larger area due to the transition of the Fe element to the structure.

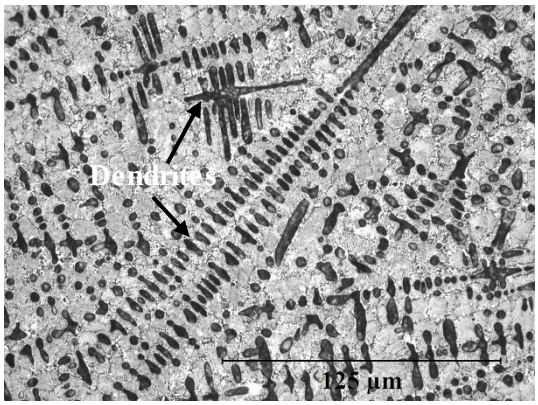

Figure 6. OM photograph of S2 x500.

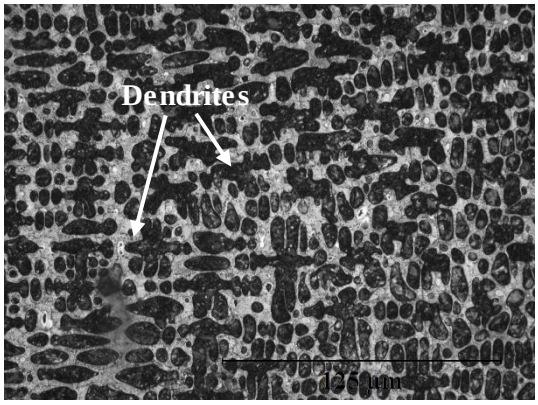

Figure 7. OM photograph of S3 x500.

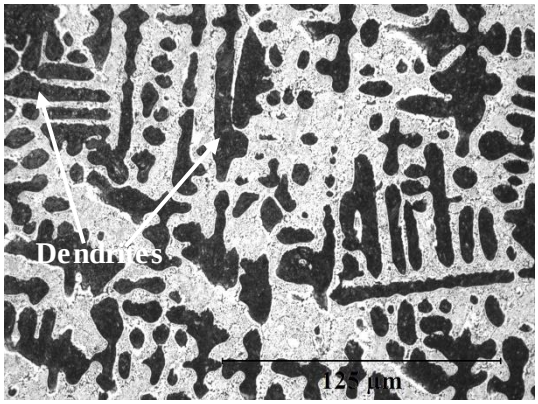

Figure 8. OM photograph of S4 x500.

Figure 11 shows the SEM photographs and EDS analyzes taken from different points of the coating areas. According to the EDS results taken from point 1 in Figure 11a, this point contains (%-wt.) 32.82Fe-31.23Cr-35.95C elements.

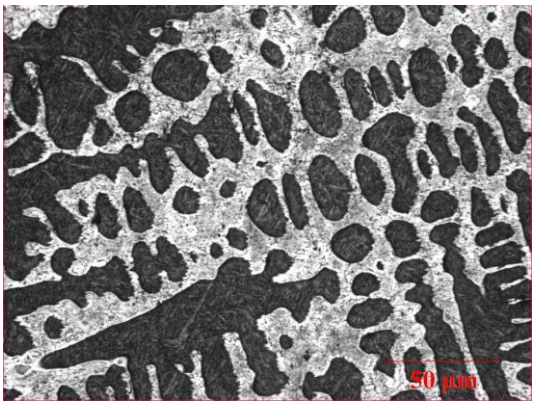

Figure 9. OM photograph of S5 x500.

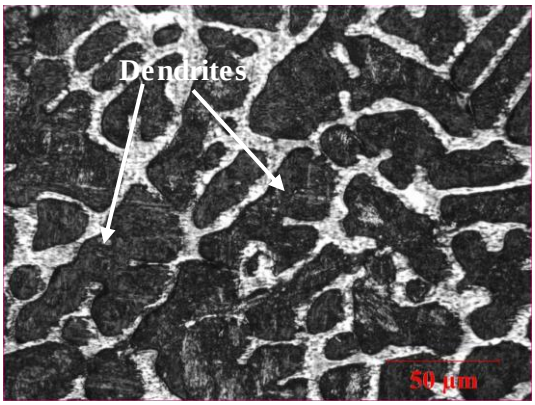

Figure 10. OM photograph of S6 x500.

According to the Cr/Fe ratio, this phase is M_7C_3 (M=Fe, Cr) carbide. The phase at point 2 contains (%-wt.) 38.43Fe-20.82Cr-40.75C elements.

It is thought that from EDS and XRD results, this phase is (Cr, Fe)B boride. According to the EDS results taken from dendrites, point 3 in Figure 11b contains (%-wt.) 73.24Fe-8.54Cr-18.22C elements, point 5 in Figure 11c contains (%-wt.) 65.84Fe-4.76Cr-29.4C elements, point 7 in Figure 11d contains (%-wt.) 66.52Fe-5.08Cr-28.4C elements, point 9 in Figure 11e contains (%wt.) 58.92Fe-4.72Cr-36.36C elements and point 11 in Figure 11f contains (%-wt.) 67.15Fe-3.13Cr-29.71C elements. Also according to the EDS results taken from eutectics, area 4 in Figure 11b contains (%-wt.) 63.50Fe-16.51Cr-19.99C elements, area 6 in Figure 11c contains (%-wt.) 68.79Fe-10.49Cr-20.72C elements, area 8 in Figure 11d contains (%-wt.) 64.69Fe-9.37Cr-25.94C elements, area 10 in Figure 11e contains

(%-wt.) 59.77Fe-10.16Cr-30.08C elements and area 12 in Figure 12f contains (%-wt.) 68.09Fe-9.87Cr-22.04C elements. As can be seen from the EDS analysis results, similar structures are in different chemical compositions due to different melting intensities with the change of heat input.

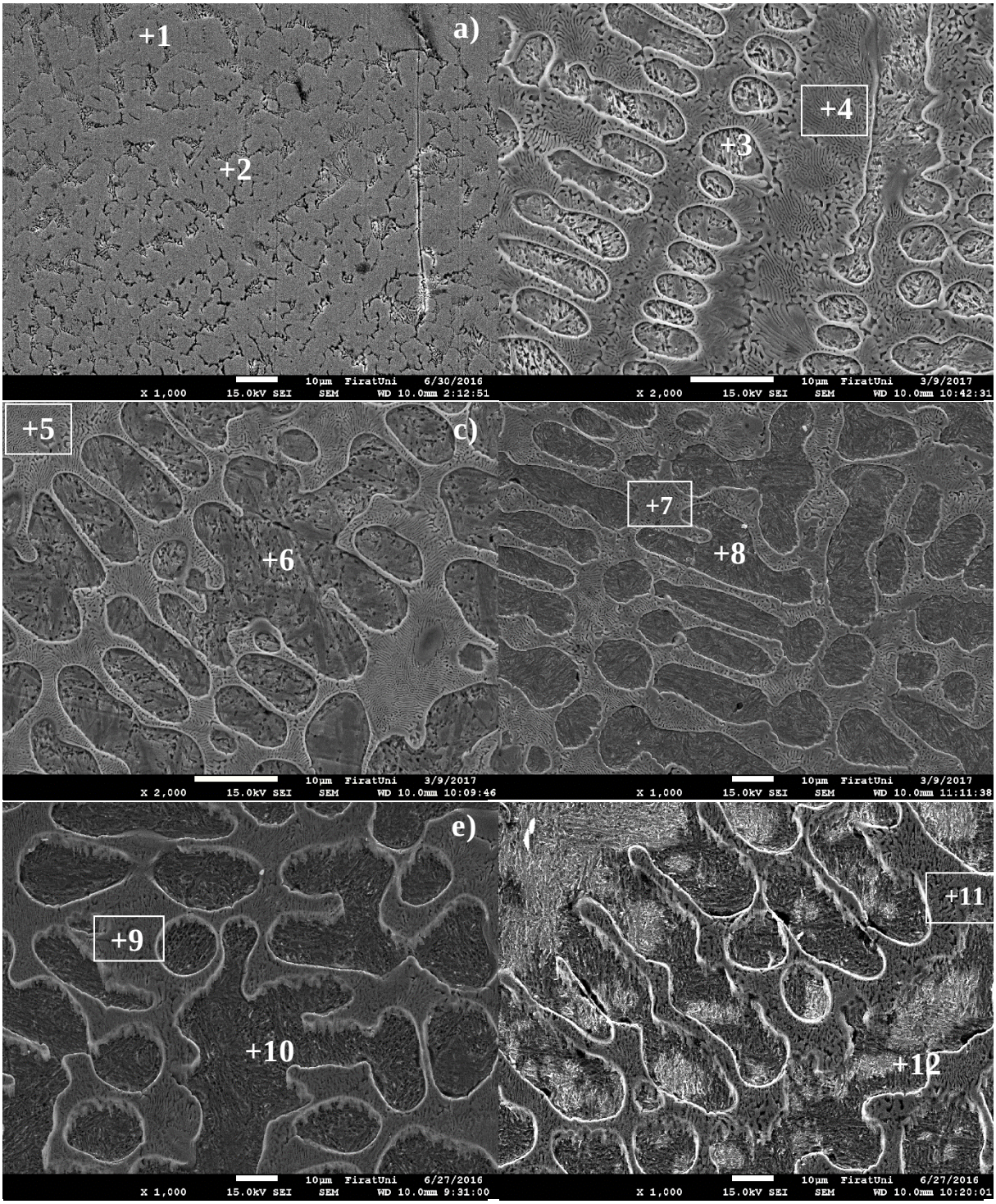

Figure 11. SEM photograps of the coating layers **a)** S1 (x1000), **b)** S2 (x2000), **c)** S3 (x2000), **d)** S4 (x1000), **e)** S5 (x1000) and f) S6 (x1000).

3.2 Microhardness

The microhardness distribution of the coating layers are given in Figure 12. It was seen that the microhardness of the coating layers are higher than the substrate material due to the hard borides and carbides in their structures. It was seen that the average microhardness of the coating layers varied from 621 to 1096 HV and decreased with increasing heat input. The highest micro - hardness value was measured as 1254 HV in sample S1, which was coated with the lowest heat input.. The average microhardness values of the coating layers are 1096 HV, 991 HV, 858 HV, 812 HV, 703 HV and 621 HV for samples S1, S2, S3, S4, S5, S6 respectively

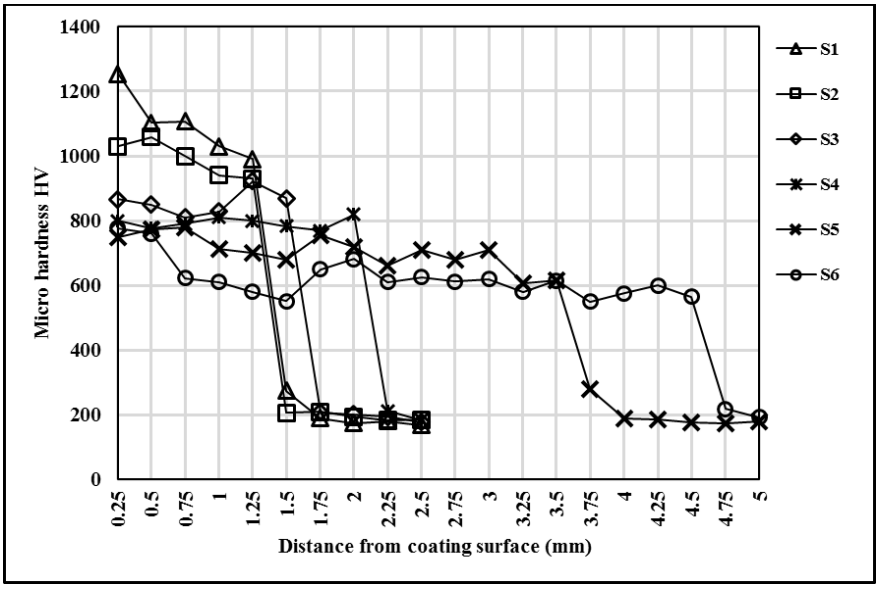

Figure 12. Microhardness distribution of coating layers

3.3. Wear and Friction

At 19.62 N, 39.24 N and 58.86 N normal load the change in wear losses according to the sliding distance are given in Figures 13-15 respectively. It was found that the wear losses of coated samples are less than the substrate material at all load values. As the average microhardness of the coating layers decreased, wear losses increased. The sample with the best wear resistance at all load values is the sample S1, which is coated with the lowest heat input and has the highest average hardness. The sample with the lowest wear resistance is the sample S6, which is coated with highest heat input and is the softest sample. At 19.62 N load, the wear resistances of the other specimens except the specimens coated with high heat input (S5 and S6), tending to increase according to the sliding distance (Figure 13).

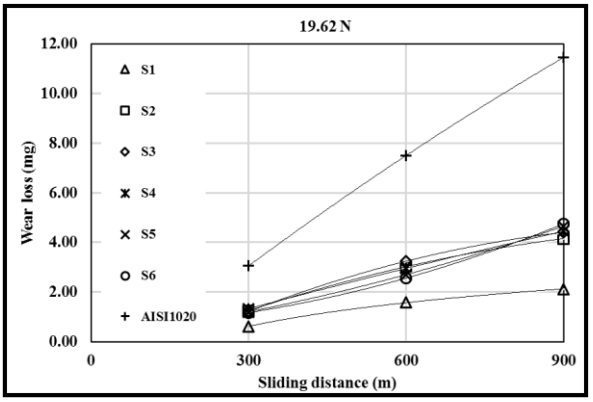

Figure 13. Wear losses at 19.62 N load.

At 39.24 N load, the wear resistances of all samples decreased when the sliding distance increased to 600 m and increased when the sliding distance increased to 900 m (Figure 14).

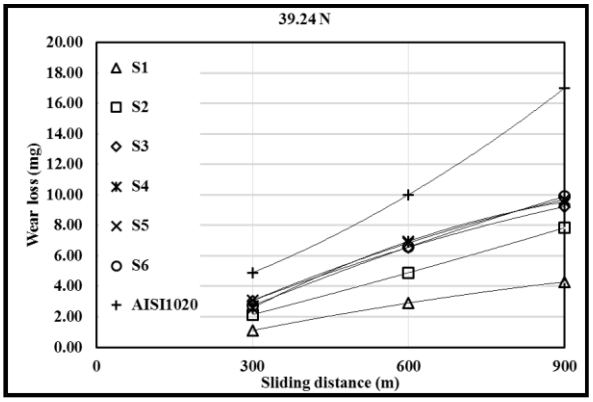

Figure 14. Wear losses at 39.24 N load.

At 58.86 N load (Figure 15), the wear resistance of the S6, which is coated by the highest heat input, is increased according to the sliding distance. The wear resistances of the S1-S5 decreased with the increase of the sliding distance to 600 m and increased when the sliding distance increased to 900 m.

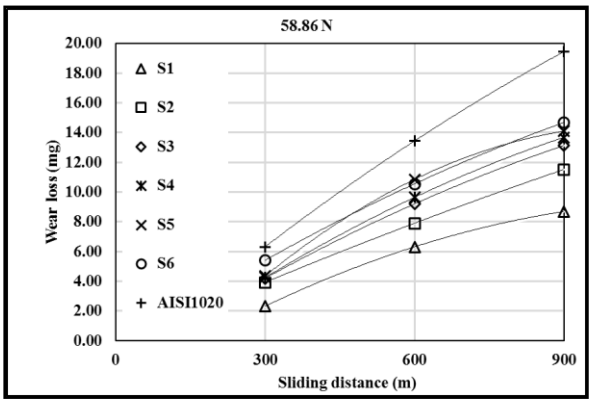

Figure 15. Wear losses at 58.86 N load.

The change in wear losses according to the normal load is given in Figure 16. As it seen, the wear resistance of the S1, which has the highest average microhardness, decreases as the load increases. The wear loss of the S2, which has an average micro hardness close to this sample, increases with increasing load. The wear resistances of the other samples decreased when the load increased to 39.24 N and increased when the load increasedto 58.86 N.

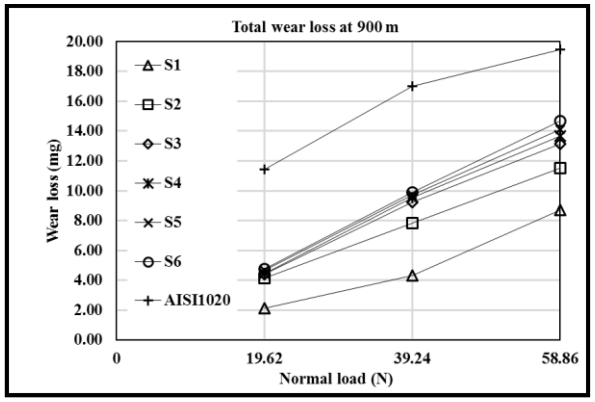

Figure 16. Wear losses according to normal load.

In Figure 17, the variation of average friction coefficients ($\mu_{ave.}$) according to the load is shown. The samples with high average microhardness have higher $\mu_{ave.}$ values and as the heat input increases, the μ_{ave} values decrease at all load. The $\mu_{ave.}$ values of the samples vary between 0.619 - 0.806 at 19.62 N load, 0.665 - 0.78 at 39.24 N load and 0.601 - 0.74 at 58.86 N load.

At 19.62 and 39.24 N load, the average coefficient of frictions of all samples are lower than the AISI 1020. The average friction coefficients of S1-S5 at 58.86 N load are higher than the AISI 1020. Also S6's average friction coefficient is close but higher than the AISI 1020 at 58.86 N load.

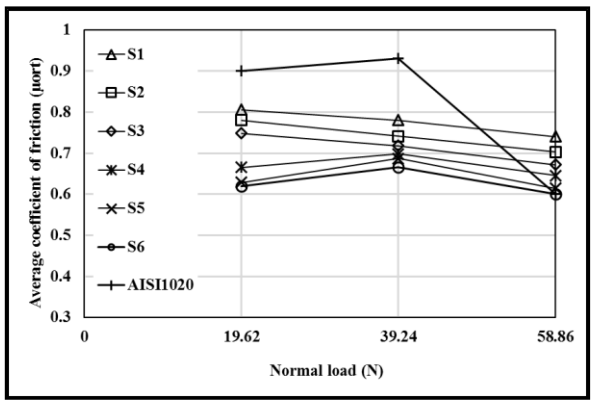

Figure 17. The variation of average friction coefficients according to load.

The wear surface SEM photographs of the samples worn at most (S6), at least (S1) and the substrate material at each load are shown in Figure 17. Significant amounts of the material were lost at all loads from substrate (Figure 17a-

c). In the substrate material, it was determined that the particles broken from the surface were removed from the surface at 19.62 N and 39.24 N load while the broken particles were plastered to the grooves formed on the surface at 58.86 N load due to the high temperature. Peeling and craters were observed on the worn surface of the substrate material at low load. Again, the roughness of the surface at this load is much higher because the broken particles did not plaster to the surface due to the low load (Figure 17a). Wide and deep craters were observed on the worn surfaces at medium and high loads. Wear was usually in the form of scraping. According to the EDS results taken from the wear surfaces of the substrate material, oxidation occurred on the worn surfaces and these oxides were plastered to the surface at a high load and reduced the friction coefficient. If S1's worn surfaces investigated, it is seen that grooves formed on the surface at 19.62 and 39.24 N load (Figure 17d and e). At 58.86 N load, the abrasion is more of a scrape, and scraping pits formed on the surface (Figure 17f). As it seen from S6's worn surface photograps, grooves and spalling formed at 19.62 N load (Figure 17g). At 39.24 N load, it is seen that the particles have been stripped off from the surface and scraping pits and spalling formed on worn surface (Figure 17h). At 58.86 N load, the grooves flattened with increasing wear (Figure 17ı).

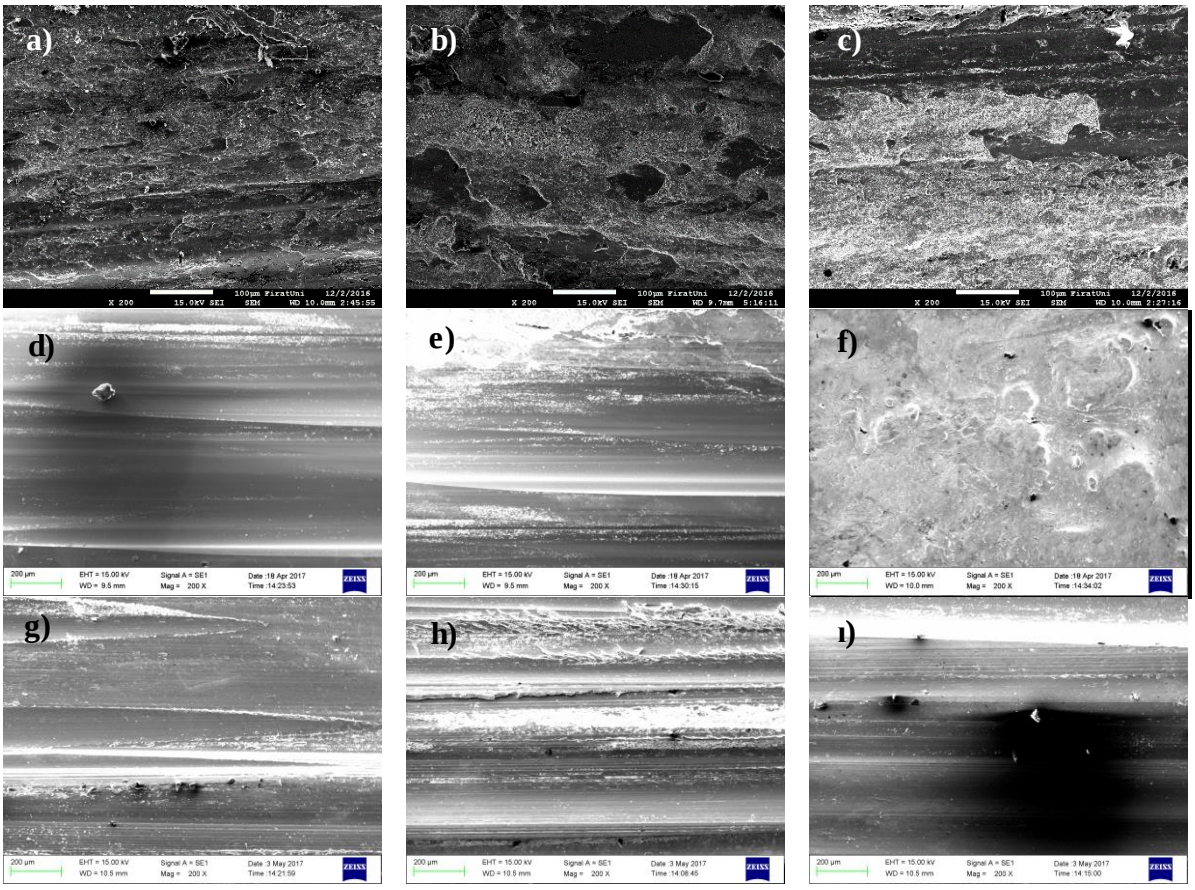

Figure 18. SEM photographs of the wear surface **a)** AISI 1020 19.62 N, **b)** AISI 1020 39.24 N, **c)** AISI 1020 58.86 N, **d)** S1 19.62 N, **e)** S1 39.24 N, **f)** S1 58.86 N, **g)** S6 19.62 N, **h)** S6 39.24 N and **ı)** S6 58.86 N.

Acknowledgment

The authors thanks to the Firat University Research Fund (FUBAP-MF.15.09) for their financial contribution to this research.

4. Conclusions

- The surface of AISI 1020 was successfully modified with Fe-Cr-B-C elements by using the PTA welding method.

- Coating layers depths and interface regions heights were increase with increasing heat input.
- No porosity or cracks were found on the coating layers and interfaces.
- Coating layers were generally composed of M_7C_3 (M=Cr, Fe) carbide, (Cr, Fe)B, FeB and Fe_2B borides.
- The dendrite arms expand and stretch as the heat input increases.
- The average microhardness of the coating layers varies from 621 to 1096 HV and decreases as the heat input increases. The highest microhardness value was measured at 1254 HV in sample, which was coated with the lowest heat input.
- The total wear loss of the coated samples was observed to be lower when compared to AISI 1020 steel at 19.62 N, 39.24 N and 58.86 N load. As the average microhardness of the coating layers decreased, wear losses increased.
- The samples with high average microhardness have higher $\mu_{ave.}$ values and as the heat input increases, the μ_{ave} values decrease.

5. References

1. Gou, J., Lu, P., Wang, Y., Liu, S., and Zou, Z. (2016). Effect of nano-additives on microstructure, mechanical properties and wear behaviour of Fe–Cr–B hardfacing alloy. *Applied Surface Science*, **360**: 849-857.

2. Buchely, M., Gutierrez, J., Leon, L., and Toro, A. (2005). The effect of microstructure on abrasive wear of hardfacing alloys. *Wear*, **259**(1): 52-61.

3. Tarng, Y., Juang, S., and Chang, C. (2002). The use of grey-based Taguchi methods to determine submerged arc welding process parameters in hardfacing. *Journal of Materials Processing Technology*, **128**(1): 1-6.

4. Chatterjee, S. and Pal, T. (2003). Wear behaviour of hardfacing deposits on cast iron. *Wear*, **255**(1): 417-425.

5. Saha, A. and Mondal, S.C. (2016). Multi-objective optimization in WEDM process of nanostructured hardfacing materials through hybrid techniques. *Measurement*, **94**: 46-59.

6. Korkut, M., Yilmaz, O., and Buytoz, S. (2002). Effect of aging on the microstructure and toughness of the interface zone of a gas tungsten arc (GTA) synthesized Fe–Cr–Si–Mo–C coated low carbon steel. *Surface and Coatings Technology*, **157**(1): 5-13.

7. Wang, Z.-T., Zhou, X.-H., and Zhao, G.-G. (2008). Microstructure and formation mechanism of in-situ TiC-TiB2/Fe composite coating. *Transactions of Nonferrous Metals Society of China*, **18**(4): 831-835.

8. Wu, Q., Li, W., Zhong, N., Gang, W., and Haishan, W. (2013). Microstructure and wear behavior of laser cladding VC–Cr7C3 ceramic coating on steel substrate. *Materials & design*, **49**: 10-18.

9. Wieczerzak, K., Bala, P., Stepien, M., Cios, G., and Koziel, T. (2016). Formation of eutectic carbides in Fe–Cr–Mo–C alloy during non-equilibrium crystallization. *Materials & design*, **94**: 61-68.

10. Yang, J., Hou, X., Zhang, P., Zhou, Y., Yang, Y., Ren, X., and Yang, Q. (2016). Mechanical properties of the hypereutectoid Fe–Cr–C hardfacing coatings with different nano-Y2O3 additives and the mechanism analysis. *Materials Science and Engineering: A*, **655**: 346-354.

11. Buytoz, S., Yildirim, M.M., and Eren, H. (2005). Microstructural and microhardness characteristics of gas tungsten are synthesized Fe–Cr–C coating on AISI 4340. *Materials Letters*, **59**(6): 607-614.

12. Jin, H., Rhyim, Y., Park, C., and Kim, M. (1997). Microstructure and wear-resistance of Fe-Cr-B base metamorphic alloys. *Metals and Materials*, **3**(1): 60-64.

13. Jin, H., Park, C., and Kim, M. (2001). In situ TEM heating studies on the phase transformation of metastable phases in Fe–Cr–B alloy spray coatings. *Materials Science and Engineering: A*, **304**: 321-326.

14. Jin, H., Rhyim, Y., Hong, S., and Park, C. (2001). Microstructural evolution of the rapidly quenched Fe–Cr–B alloy thermal spray coatings. *Materials Science and Engineering: A*, **304**: 1069-1074.

15. Manna, I., Chattopadhyay, P., Banhart, F., Croopnick, J., and Fecht, H.-J. (2008). Microstructural evolution of wear-resistant FeCrB and FeCrNiCoB coating alloys during high-energy mechanical attrition. *Wear*, **264**(11): 940-946.

16. Yüksel, N. and Şahin, S. (2014). Wear behavior–hardness–microstructure relation of Fe–Cr–C and Fe–Cr–C–B based hardfacing alloys. *Materials & design*, **58**: 491-498.